ASME Journal of Engineering for Gas Turbines and Power
Online journal at:
https://asmedigitalcollection.asme.org/gasturbinespower

R. Meloni[1]
Baker Hughes,
Florence 50127, Italy
e-mail: roberto.meloni@bakerhughes.com

G. Babazzi
Baker Hughes,
Florence 50127, Italy

N. Giannini
Baker Hughes,
Florence 50127, Italy

S. Castellani
Department of Industrial Engineering,
University of Florence,
Florence 50121, Italy

P. C. Nassini
Department of Industrial Engineering,
University of Florence,
Florence 50121, Italy

A. Picchi
Department of Industrial Engineering,
University of Florence,
Florence 50121, Italy

S. Galeotti
Department of Industrial Engineering,
University of Florence,
Florence 50121, Italy

R. Becchi
Department of Industrial Engineering,
University of Florence,
Florence 50121, Italy

A. Andreini
Department of Industrial Engineering,
University of Florence,
Florence 50121, Italy

Thickened Flame Model Extension for Dual Gas Turbine Combustion: Validation Against Single Cup Atmospheric Test

The development of predictive combustion models is more and more strategic in the design definition of gas turbine (GT) combustor. The thickened flame model (TFM), despite its high computational cost, is one of the most accurate approach available in literature since it can naturally take into account the nonequilibrium effects into the flame brush (i.e., strain and heat losses) as well as preferential diffusion when hydrogen is employed. Conversely, the original formulation of this combustion model needs several adjustments to accommodate the properties of the mixture when different streams of fuels and/or oxidizers are present in the system. The present work represents a first step in the extension of this combustion model to handle multiple streams of fuels and oxidizers. More specifically, an industrial burner fed with two different fuel streams and air as oxidizer is considered. The pilot fuel line is fed with microhydrogen injections with the aim to enhance the lean blow-out margin, while the main one is with pure methane. Dedicated tests are performed at the Technology for High Temperature laboratory (University of Florence) to retrieve the main information characterizing the burner (emissions, temperature, and pressure pulsations) as well as OH chemiluminescence for the flame shape and position at the same operating conditions. The comparison between the numerical results and the experimental data will provide highlights about the ability of the extended-TFM to capture the main features of the flame stabilization mechanisms.* [DOI: 10.1115/1.4066511]

Introduction

The large-eddy simulation (LES) models represent nowadays not only a tool for the verification of a specific gas turbine (GT) combustor concept but also a design method to be exploited at any level of the development. Such trend will surely benefit of higher and higher computational power allowing the modeling of detailed geometries along extremely fine computational grids covering the wide range of turbulence and chemistry scales associated with the fuel oxidation [1]. Regarding the combustion codes, the availability of extremely efficient architectures will enable the employment of more sophisticated and computationally expensive models rising the reliability of the simulations and enabling the virtual prototyping of the real hardware [2].

Among the several combustion models actually present in literature, the artificially thickened flame model (TFM) [3,4] represents one of the most accurate in the LES context, despite its high demanding computational cost due to the solution of a transport equation for each species. In fact, born to handle perfectly premixed system through global reaction mechanisms, the TFM is actually

Turbo Expo, June 24–28, 2024. GT2024.
[1]Corresponding author.
Manuscript received July 9, 2024; final manuscript received July 11, 2024; published online October 15, 2024. Editor: Jerzy T. Sawicki.

used along both skeletal and detailed chemistry sets made of dozen of species and hundreds of reactions [5–7]. The complexity of this model lays not just in the solution of many more transport equations associated with the chemistry but also in the spatial discretization requirements. From the theoretical standpoint, each species profile should be resolved with accuracy in the artificially thickened flame front, including the radicals taking part to the fuel consumption. Especially when a complex system is simulated at high pressure–high oxidizer temperature typical of modern GT combustors, the grid requirements can be hard to be reached [8] since the flame front thickness is of the order of magnitude of microns.

The development of a TFM-based model able to accurately describe stratified and nonpremixed flames was recently introduced in literature. While Cuenot et al. demonstrated the inapplicability of the TFM to pure diffusive cases [9], Aniello et al. [10] and Castellani et al. [8,11] leverage a flame index (FI) to identify the premixed combustion regime where the TFM is applied. The latter approach, that will be extensively described in the next paragraphs as one of the adopted model in this work, provides a more physical insight to such TFM-based model when it has to be employed for the investigation of industrial hardware.

Despite the TFM can manage any composition for both the fuel and the oxidizer side, the calculation of the mixture properties when multiple streams have to be considered is an aspect that has not been fully investigated in the present literature. Recently, Mocquard et al. [12] conceived a formulation to calculate the properties of the mixture in a vitiated environment typical of postcombustors to tune a two-steps chemistry for kerosene combustion. Indeed, the laminar flame speed (LFS) and the laminar flame thickness (LFT), concurring in the calculation of the efficiency function (E) and the thickening factor (F) in the TFM, are not anymore a simple function of the equivalence ratio when the system is characterized by different streams of fuel and/or oxidizers. Since the performances of this combustion model are dependent on both these parameters, it is crucial to properly calculate them according to the actual composition at the cell level. In the present paper, a theoretical formulation will be presented to cover this lack. Despite the test case that will be used as validation represents a dual-gas application, the formulation will be presented in a general form since it can be applied to any system characterized by multiple fuel–oxidizer inlets. It must be finally remarked that for cases having different compositions at the boundaries (multifuels or multi-oxidizers problems in the same simulation), the combustion models based on the species transport approach are the only option since the ones relying on the chemistry pretabulation, like the flamelet generated manifold, are not always able to handle this kind of problems.

The paper starts describing the mathematical formulation of both the combustion model and its extension conceived to properly calculate the mixture properties based on the cell-based elemental mass fraction. This approach will be validated against experimental data acquired along an atmospheric test rig operated in a dual-gas mode with air as oxidizer. The peculiarities of the experimental setup will be described in a dedicated paragraph as well as the detailed operating conditions employed to retrieve the data. The Results and Discussion section will compare the numerical findings with the experimental evidence highlighting the potential aspects where the model can be further improved. A detailed postprocessing regarding the flame stabilization regions will be provided to highlight the anchoring mechanisms of the flame, especially close the pilot jets where hydrogen is employed to enhance the lean blow-out margin with respect to the standard application with natural gas.

Numerical Modeling

Combustion Model: Thickened Flame Model Extension. From a mathematical standpoint, the transport equation of the generic species mass fraction φ can be written in the TFM context as follows:

$$\frac{\partial \bar{\rho}\,\tilde{\varphi}}{\partial t} + \frac{\partial \bar{\rho}\,\tilde{u}_j\,\tilde{\varphi}}{\partial x_j} = \frac{\partial}{\partial x_j}\left(\bar{\rho}\left(EFD + (1-\Omega)D_t\right)\frac{\partial \tilde{\varphi}}{\partial x_j}\right) + \frac{E}{F}\dot{\omega}(\tilde{\varphi}) \tag{1}$$

where E, F, and Ω are the efficiency function, the thickening factor, and the flame sensor, respectively. The efficiency function from Colin et al. [3] is calculated according to the following equation:

$$E = \frac{1 + \alpha\Gamma_0 \dfrac{u'_{\Delta_e}}{s_l^0}}{1 + \alpha\Gamma_1 \dfrac{u'_{\Delta_e}}{s_l^0}} \tag{2}$$

with the dilatation-free velocity at the test filter u'_{Δ_e} calculated through the formulation of Durand and Polifke [13], leveraging a scale similarity assumption (Eq. (3))

$$u'_{\Delta_e} = c\Delta\left|\nabla \times \tilde{\boldsymbol{u}} - \nabla \times \widehat{\tilde{\boldsymbol{u}}}\right| \tag{3}$$

This approach is implemented by the authors in the commercial code ANSYS FLUENT through a dedicated user defined function (UDF). The maximum thickening factor ($F_{\max}$) is calculated considering a number of points in the flame thickness (N) equal to 4 in this case. Its value depends on the characteristic size of the mesh (Δx) and the local value of the LFT (Eq. (4))

$$F_{\max} = \frac{\Delta x N}{\mathrm{LFT}(\Phi)} \tag{4}$$

Basing on this value, the dynamic thickening factor that allows the application of the artificial thickening only where the flame front is located is calculated as

$$F = \Omega(F_{\max} - 1) + 1 \tag{5}$$

with the flame sensor Ω identified through the reaction involving hydrogen with the radical OH, the best to detect the flame front location. In the extended version of the TFM, all the transport equations of the chemical species are dependent on the normalized FI, defined according to the following equation:

$$\mathrm{FI} = \frac{\nabla Y_F \cdot \nabla Y_{\mathrm{ox}}}{|\nabla Y_F \cdot \nabla Y_{\mathrm{ox}}|} \tag{6}$$

In this study, the fuel mass fraction is defined as $Y_F = Y_{\mathrm{H2}} + Y_{\mathrm{CH4}}$. When the fuel mass fraction gradient ∇Y_F is aligned with the oxidizer mass fraction gradient ∇Y_{ox}, i.e., positive FI, the partially premixed regime is detected leading to the use of the standard TFM formulation. The flame propagation speed is fixed, and the reaction source term is chemically limited in these conditions. Conversely, when the diffusive combustion regime is identified (FI < 0), the transport equations are closed with a finite rate (FR) assumption, the most suitable when the flame is diffusion-controlled and stabilizes mainly at the stoichiometric isosurface. In the latter condition, the efficiency function and the dynamic thickening factor are imposed equal to 1, and no thickening is applied to the flame front. All these steps are performed in a dedicated UDF acting as an odd-on of the standard TFM. Regarding the chemistry set, a skeletal mechanism made of 19 species–119 reaction presented in Ref. [8] and derived from the San Diego mechanism [14] is used.

Theoretical Formulation of the Dual Fuel/Dual Oxidizer Thickened Flame Model Extension. Having multiple streams of fuels and/or oxidizers has two main consequences for the combustion model. As previously stated, the first is the determination of the mixture properties in terms of LFS and LFT. Second is the calculation of the flame sensor Ω. Both these aspects are resolved leveraging a pretabulation approach. The details will be provided in the Reconstructed Unburnt Composition Calculation, Flame Sensor, and Pretabulation of the Mixture Properties and the Maximum Reaction Rate sections.

Reconstructed Unburnt Composition Calculation. The elemental mass fraction in a cell of a reactive simulation can be easily calculated through the following equation:

$$Z_i = W_i \sum_{m=1}^{M} \frac{a_{i,m} Y_m}{W_m} \tag{7}$$

with W_i is the molecular weight of the element i, M is the total number of species of the chemistry set, $a_{i,m}$ is the number of elements i contained in the generic species m, and Y_m is its mass fraction. Can Z_i derive from any combination of unburnt species? The answer is no: its value is a direct consequence of the boundary conditions of the problem. Since the elemental mass fractions must be conserved, an alternative formulation of the elemental mass fractions, function of the unburnt species only, can be

$$Z_i = W_i \sum_{n=1}^{N} \frac{a_{i,n} Y_n^u}{W_n} \tag{8}$$

where N is the total number of the unburnt species, $a_{i,n}$ is the number of i elements contained in the unburnt species n, and Y_n^u is the corresponding mass fraction. The latter set of equations has also to consider the "constrains" that define the specific case under investigation. For example, when the oxidizer is simply air, the ratio between the oxygen and the nitrogen mass fractions is fixed. If the oxidizer is a generic exhausted gas recirculation, the ratio between CO_2 and O_2 is known and represents a constrain that can be used to make the definition of the equations system unique. In this way, the N unknowns of the problem (Y_n^u) can be easily determined leveraging the system of equations from Eq. (7), solving the following system:

$$\begin{pmatrix} W_1 \frac{a_{1,1}}{W_1} & \cdots & W_i \frac{a_{1,N}}{W_N} \\ \vdots & \ddots & \vdots \\ W_1 \frac{a_{1,1}}{W_1} & \cdots & W_i \frac{a_{I,N}}{W_N} \end{pmatrix} \begin{pmatrix} Y_1^u \\ \vdots \\ Y_N^u \end{pmatrix} = \begin{pmatrix} Z_1 \\ \vdots \\ Z_I \end{pmatrix} \tag{9}$$

Flame Sensor. In the original formulation of the dynamically thickened flame model, the flame sensor is employed to identify the heat release zone and apply the thickening only inside the flame front, leaving the rest of the domain unaffected. The mathematical definition of the flame sensor is based on the reaction rate of the reaction selected by the user as representative of the heat release rate, usually involving a radical (Eq. (10))

$$\Omega = \tanh\left(\beta \frac{|\dot{\omega}_i|}{\max\left(|\dot{\omega}_i|\right)}\right) \tag{10}$$

where β is a constant of the model, and $\max\left(|\dot{\omega}_i|\right)$ is the maximum of the reaction rate inside the domain. Especially in the context of the dual-gas applications, the large variability in the local mixture composition can lead to significant changes in the rate of the reference reaction. So, it is preferable to perform the normalization through the maximum reaction rate of the reference reaction calculated at the local value of unburnt mixture compositions $\overline{\dot{\omega}_T}$ as follows:

$$\Omega^T = \tanh\left(\beta \frac{|\dot{\omega}_i|}{|\overline{\dot{\omega}_T}|}\right) \tag{11}$$

Such information, as well as the LFS and LFT, can be easily calculated a priori and stored in a look-up table. The query process performed during the simulation is explained in the next subparagraph.

Pretabulation of the Mixture Properties and the Maximum Reaction Rate. A freely propagating flame model is employed in CANTERA [15] at the same operating pressure and the same oxidizer temperature at which the computational fluid dynamics (CFD) simulation has to be performed. The fuels and the oxidizers compositions have to be specified as an input as well as the number of the reaction considered as representative of the heat release rate for the calculation of $\overline{\dot{\omega}_T}$. It is preferable (but not mandatory) to use the same chemistry set of the CFD also in this stage.

The variability ranges of the fuels mass fractions and the number of points used to discretize these ranges have to be specified in order to define a matrix of fuel concentrations. Each point of the matrix represents a possible combination of the fuel concentrations. All these combinations are provided as input to the freely propagating flame from which the LFS, LFT, and the maximum reaction rate $\overline{\dot{\omega}_T}$ are calculated. These preliminary maps are finally further refined interpolating between the calculated points and stored in a table that is read during the CFD simulation. Figure 1 provides an example of these maps for a dual-gas case having pure hydrogen and pure methane as fuels and air as oxidizer.

More generally, in a dual-gas and dual-oxidizers (or in an n-gas and n-oxidizers) system, the above described procedure must be repeated also in the oxidizers space. This means that all the possible combinations of the oxidizer mass fractions (according to the user defined number of points) must be taken into account and, for each possible combination, the above described sweeps in the fuel's variability must be considered. The total number of simulations to be performed in CANTERA are

$$\prod_{i=1}^{N\text{fuel}} n_{f\,i} \left(\prod_{j=1}^{N\text{oxid}-1} n_{\text{ox}\,j} \right) \tag{12}$$

with Nfuel is the total number of separate fuel inlets, Noxid is the total number of different oxidizers in the system, and n_f, n_{ox} is the number of point used to discretize the variability range of each stream. To provide an example, in a dual-gas and dual-oxidizer case,

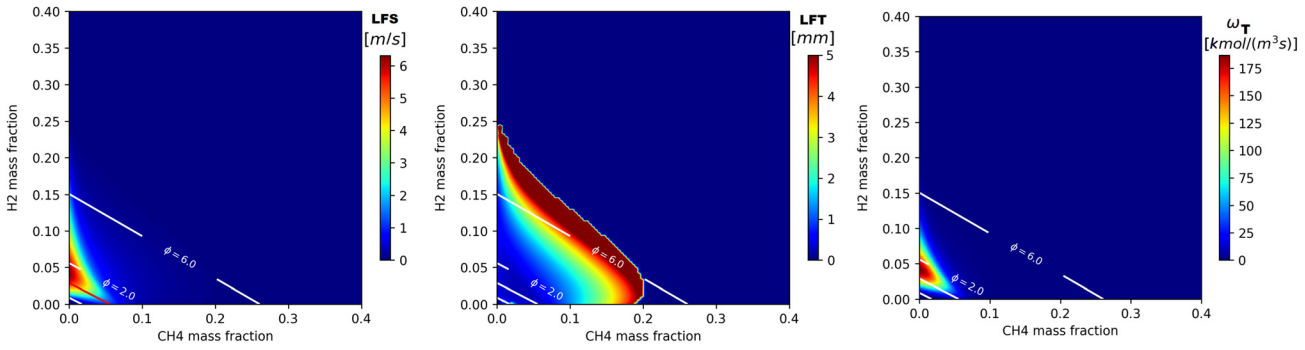

Fig. 1 Pretabulated maps of laminar flame speed (left), LFT (center), and maximum reaction rate $\overline{\dot{\omega}_T}$ (right) function of the recalculated local mass fractions of the fuels. In this example, the two fuels are pure hydrogen and pure methane, while the oxidizer is air.

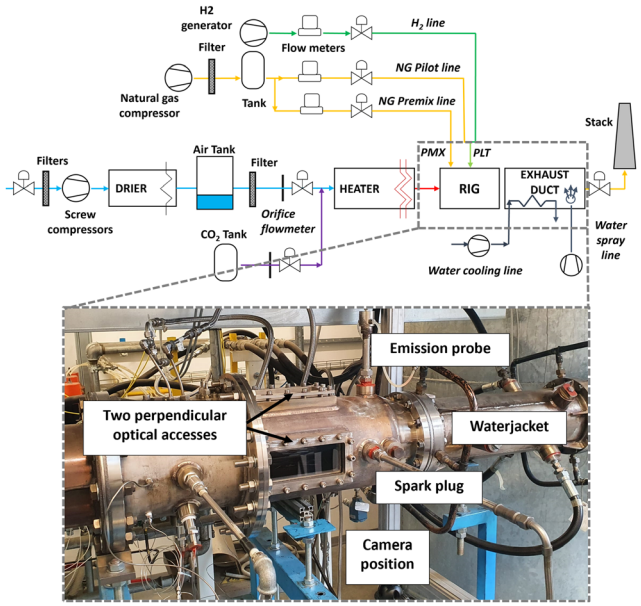

Fig. 2 Layout of the test facility (top) and close-up of the combustion test article with the optically accessible liner (bottom)

each CANTERA simulation requires three inputs: the fuel mass fractions and the mass fraction of one of the oxidizer (the second can be calculated as complement to 1). The total number of simulations to be performed in CANTERA are $n_{f1} \cdot n_{f2} \cdot n_{o1}$.

During the CFD simulation, another UDF calculates the reconstructed unburnt mass fractions of the fuels according to the procedure described in the Reconstructed Unburnt Composition Calculation section and uses these values to query the pretabulated table to provide cell-by-cell the three quantities.

Test Rig and Operating Conditions

The test rig located at the Technology for High Temperature Lab of the University of Florence (Fig. 2) is equipped with an electric heater of 600 kW able to warm up a maximum mass flow rate of the oxidizer equal to 1 kg/s up to 400 °C. The desired oxidizer composition can be obtained mixing the dried, filtered, and compressed air with CO_2 stored in separated tanks. The air and the CO_2 mass flow rates are usually adjusted to reach the target of oxygen in the stream. The oxidizer can be considered perfectly mixed when it reaches the burner since the CO_2 is injected right before the electric heater inlet, so well upstream the combustion section. Entering the rig, the oxidizer mass flow rate splits in two main flows: one directed through the swirler and the second in the sleeve between the quartz and the external casing to cool down the quartz and the metal liner in sequence. The rig is equipped with a maximum of three independent fuel lines, delivering a maximum of 90 $N \cdot m^3/h$ at 16 bar. In the test conditions investigated in this work, only two of them are used. Indeed, the multifuel burner has a pilot fuel line responsible for the flame stabilization injecting the fuel directly in the primary zone of the combustor and a premixed line delivering the fuel gas inside the blades of an axial swirler [16–18].

As can be seen in Fig. 2, the external casing has two optical access displaced perpendicular each other through which the liner made of quartz can be visualized. The optical access allows to perform a detailed diagnosis of the flow field though the particle image velocimetry (PIV) and the flame topology leveraging a Phantom MIRO M340 camera. In particular, the chemiluminescence is executed coupling the camera with an intensifier and an UV lens having a bandpass filter at 310±2 nm to detect the OH* signal. A 1000 Hz acquisition frequency is used to record the flame in the investigated condition along a gain equal to 5 and an exposure time of 0.5 ms. The rig can also leverage standard instrumentation like different thermocouples located at the dome plate and the metal liner downstream the quartz liner, as well as static pressure probe to monitor the pressure drop across the burner. A dynamic pressure sensor is instead used to detect any thermo-acoustic instability during the test execution. Regarding the pollutant emission measurement, a HORIBA PG300 is installed to analyze the exhausted dried gas that is sampled at about 10 ms of residence time inside the combustor. A constant temperature of 150 °C is maintained from the rig to the analyzer to avoid the condensation of the water vapor.

Table 1 Test conditions considered for the simulation

Air temperature	(K)	576
Operating pressure	(bar)	1.016
Total mass flow rate	(g/s)	320
Fuel gas temperature	(K)	323
Pilot split thermal power	(%)	15% (pure H_2)
Total thermal power	(kW)	72.2

Regarding the operating conditions, the dual-gas configuration is numerically realized feeding the premixer with methane and the pilot with hydrogen. The thermal power associated with the pilot is equal to 15% of the total. It must be mentioned that during the test, the premixer is fed with natural gas with a C_{2+} content of about 8% that during the simulation is replaced through pure methane. This is the only choice to perform the simulation with a reasonable cost since the inclusion of C_{2+} and their chemistry in the mechanism would increase the computational cost of at least 1 order of magnitude. Table 1 reports the main information about the other parameters of the test rig.

During the test, the desired flame temperature can be targeted leveraging a dedicated flow network of the rig calculating the mass flow rate of air passing through the swirler from the total mass flow rate. For confidentiality reasons, the flame temperature of the test point is not reported in Table 1.

Computational Grid and Numerical Setting

Looking at Eq. (4), it can be noticed that the spatial discretization has a direct impact on the combustion model performance. High resolutions are typically required to limit the maximum thickening factor and, at the same time, discretize the premixed flame front thickness with a sufficient number of points, as investigated by Rochette et al. [19]. This prescription is even more stringent along a skeletal mechanism since also the radicals should be properly resolved within the flame front. On the diffusive side, the grid has to be sufficiently fine to well describe the mixing among reactants. Additionally, coarse meshes are not able to correctly predict neither the total heat release rate nor the inner structure of the diffusion flame [9].

In the dual fuel case under investigation, the diffusive regime can be expected predominantly close to the pilots where the highest heat release associated with the H_2 jets has to be captured. That is why a very fine mesh (200 μm) is there adopted. Outside this region, the primary zone is instead discretized through a characteristic size of the cells of 500 μm. The primary zone is expected to be dominated by the premixed regime related to the oxidation of the mixture coming from the swirler. Adopting a value of $N = 4$, a maximum thickening factor below 8 can be reached even in those cells potentially involving H_2.

Such setting is adequate to properly resolve species profiles since the flame front has a thickness equal to the mesh size in the primary zone at the investigated operating conditions. Figure 3, also reporting the main components of the three-dimensional assembly, shows the mesh resolutions associated with the remaining part of the domain too: while the premixer has again a finer mesh (500 μm), a slightly coarser grid (800 μm) is adopted downstream the primary zone. Overall, the model consists of about 23×10^6 of polyhedral elements.

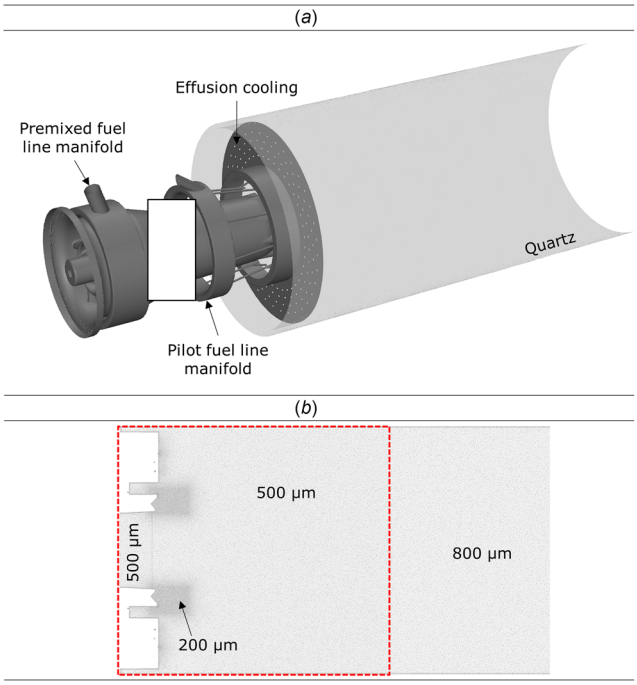

Fig. 3 (*a*) Burner-dome assembly model and (*b*) computational mesh size along the different regions of the domain

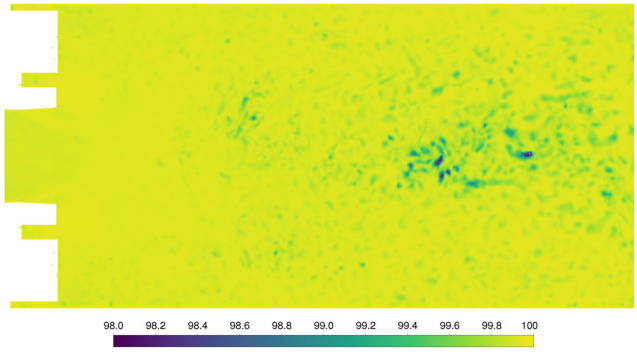

Fig. 4 Contour plot of the time-averaged Pope's criterion

The inlets are modeled through a mass flow rate boundary condition: the inclusion of both the fuel manifolds and the compressor discharge chamber upstream the swirler ensure the proper modeling of the flow fluctuations at the fuel delivery locations and at the swirler inlet, respectively. Regarding the thermal boundary conditions at the walls (meshed with three prismatic layers), a temperature is imposed in those locations where a measure from a thermocouple can be leveraged, i.e., the dome plate and the liner downstream the quartz. Regarding the latter component, the convective heat transfer coefficient of the cold side is employed (35 W/m^2 K), coupled with its bulk temperature (576 K) and a thickness of the quartz of 2.5 mm.

The wall-adapting local eddy-viscosity model [20] is used as turbulence subgrid model. Both the temporal advancement and the spatial discretization equations are solved at the second order. The fixed time-step size is chosen to limit the maximum Courant number below 5 in the entire domain.

Results and Discussion

The numerical findings will be compared with the experimental data in the next subparagraphs. The first is focused on the velocity field obtained from nonreactive conditions. The second will present the results characterizing the flame morphology and the stabilization regions.

Velocity Field. A dedicated PIV is executed at isothermal conditions with the temperature of the air set at the same value reported in Table 1. The goal is not only the validation of the flow field coming from the corresponding LES but also an evaluation of the mesh resolution, eventually used at reacting conditions. In fact, the evaluation of the spatial resolution based on the percentage of the resolved turbulent scales could be not fully exhaustive along the TFM [21]. So, the goodness of the proposed grid is measured also against the velocity field prediction in order to be more conservative. The results of the numerical simulation refer to a time-averaged solution of about three flow through times of the combustion chamber, after four flow through times of washing phase. Figure 4 reports the Pope's criterion [22] evaluated by the ratio of the resolved over the total turbulent kinetic energy, the latter being the sum of the resolved and the subgrid scales contribution

$$k_{sgs} = \left(\frac{\mu_{sgs}}{\rho l_{sgs}}\right)^2 \tag{13}$$

with μ and l the subgrid-viscosity and length scale, respectively. This contour plot demonstrates that more than 95% of the turbulent

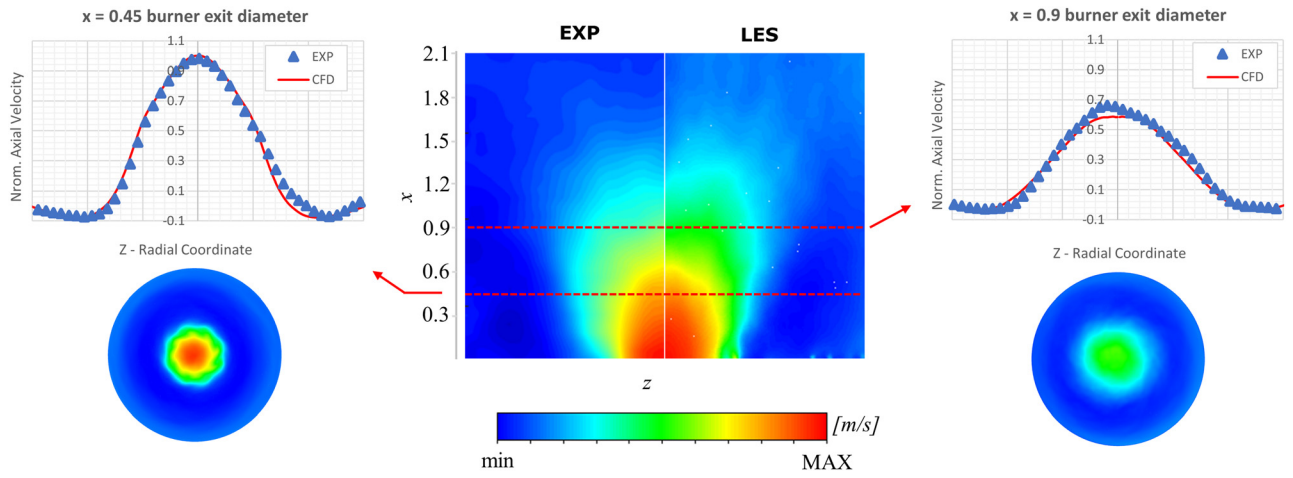

Fig. 5 Comparison between the time-averaged axial component of the velocity from the PIV (left) and the LES (right). The graphs report the velocity profiles at 0.45 and 0.9 burner exit diameter from the chamber inlet; for the numerical simulation, also the corresponding contour plots on these planes are reported. All the data are normalized against the experimental peak value.

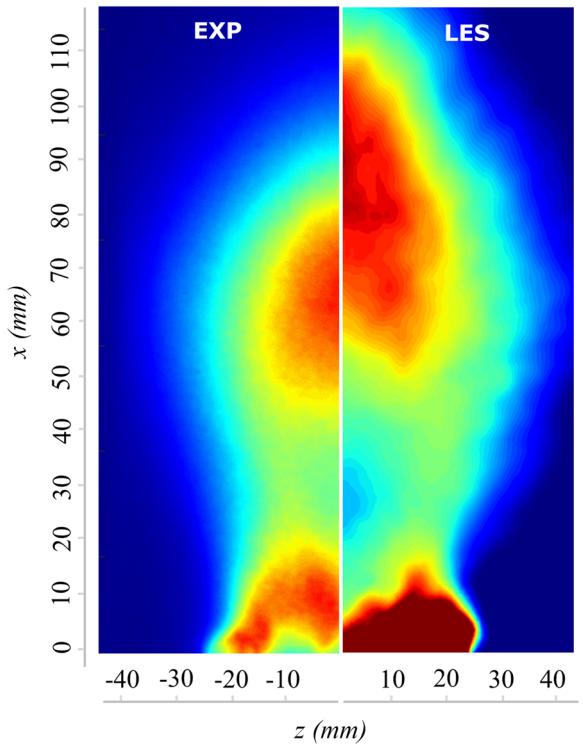

Fig. 6 Numerical line of sight of the HRR (left) versus experimental OH* line of sight (right). Dimensions are expressed as fraction of the burner exit diameter.

scales can be easily resolved in the primary zone and inside the premixer (shown only close to the exit section for confidentiality reasons) along the adopted mesh. In fact, only downstream the primary zone where the mesh resolution is coarser, the percentage of the resolved turbulent scales goes locally below 98%.

The quantitative comparison between the experimental and the numerical flow field is summarized in Fig. 5. The analysis is focused exclusively on the axial component of the velocity since the latter is the dominant one. Looking at the axial velocity on the midplane of the combustor (central image), it can be stated that there is a good agreement between experimental and the numerical maps. Since the numerical simulation predicts the same pressure drop across the burner with respect to the test (i.e., the flow function of the burner is correctly captured in this condition), the peak value of the axial velocity right downstream the burner exit is well captured. The only major discrepancy coming from the LES can be observed at a distance corresponding to about 1.2 burner exit diameter from the flame tube inlet where the axial velocity is slightly overpredicted. The two graphs reported in Fig. 5 show the comparison in terms of radial profiles at a distance corresponding to 0.45 and 0.9 burner exit diameter; for the LES, also the corresponding contour plots are shown. The numerical profiles are obtained performing a circumferential average of the axial velocity on these two planes. Overall, the model is capable to fit the experimental profiles, especially for the section at 0.45 burner exit diameter. Here, also the intensity of the recirculation zones far from the centerline seems to be well captured. The same observations can be done for the section at 0.9 burner exit diameter even if a small underprediction of the velocity peak along the centerline is detected. In conclusion, the constrains imposed by the combustion model in terms of mesh requirements lead to a spatial discretization ensuring a modest fraction of the modeled turbulent scales and a good prediction of the velocity field. Basing on these findings, the mesh is considered sufficiently fine, and no sensitivity is performed.

Flame Morphology and Stabilization Regions Analysis. Figure 6 compares the time-averaged line of sights of the heat release rate from the LES and the OH* from the test. Both pictures are normalized using their own peaks. It can be noticed from the experimental map that the flame is characterized by two stabilization regions: the first due to the H_2-pilot combustion and the second related to the premixed mixture from the premixer. Even if the peaks of these two flame fronts are quite distant and well

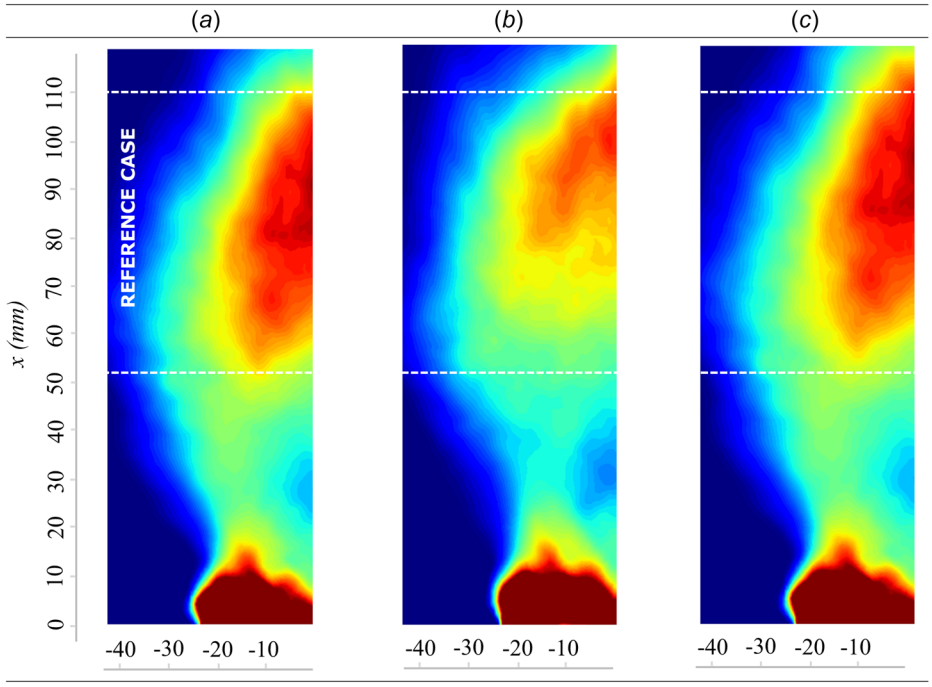

Fig. 7 HRR distribution on the midplane of the computational domain for (*a*) reference case, (*b*) increased external heat transfer coefficient for the quartz, and (*c*) increased thickening factor with the same thermal boundary of the reference case. Color bar: min (blue) is zero, and max (red) is 1. (*a*) $N = 4$/HTC 35 W/m^2 K, (*b*) $N = 4$/HTC 100 W/m^2 K, and (*c*) $N = 8$/HTC 35 W/m^2 K. (Color version online.)

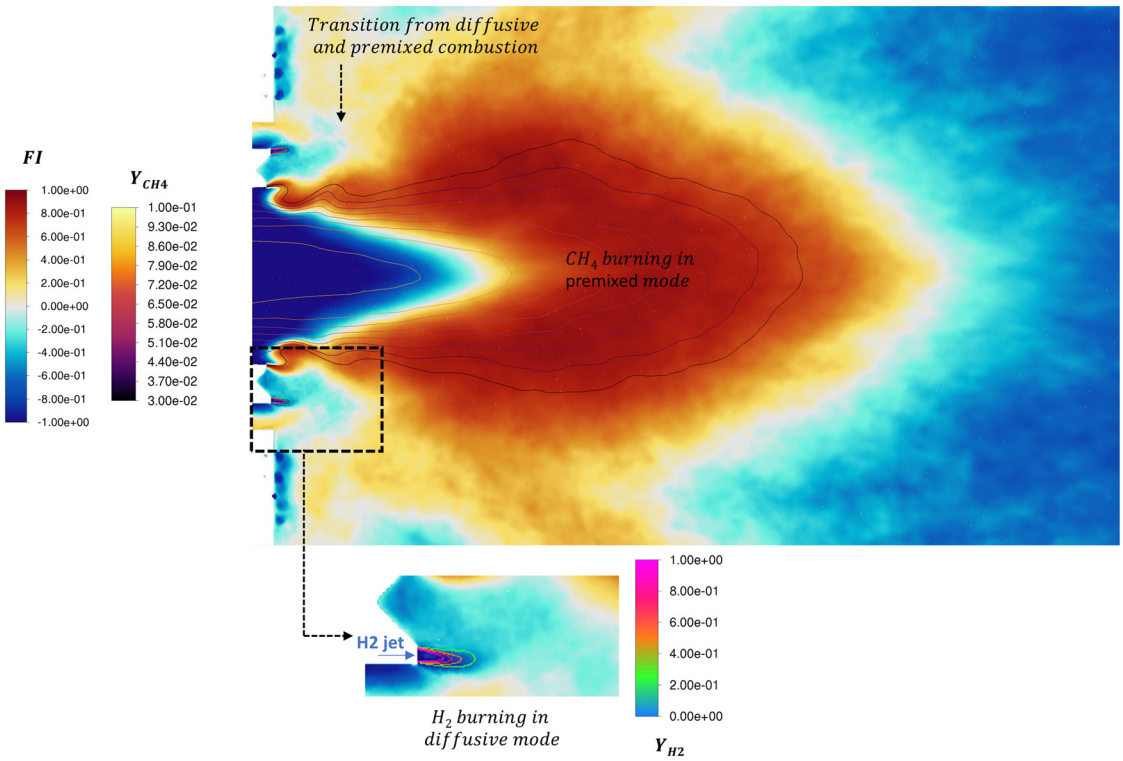

Fig. 8 Time-averaged flame index on the middle plane of the flame tube with superimposed the isolines of methane. The bottom of the figure reports a close-up of the H_2 piloted region with the corresponding isolines concentration.

separated, it can be seen that a moderate heat release is present also between them. It is hard to prove if this transition region is related mainly to H_2 or natural gas combustion since only the OH* filter is used. From the numerical standpoint, the region close to the pilot jets seems to be well captured in terms of both axial and radial extension. Instead, differently from the test, the heat release rate (HRR) peak of the pilots is quite higher than the HRR peak in the premixed part. This could be due to a rougher HRR associated with the hydrogen combustion that does not correspond to an equivalent OH* emission. The main limit of the numerical model is related to the prediction of the premixed flame length. While the initial HRR rise is slightly shifted downstream with respect to the experimental map, the LES overpredicts the premixed flame front extension. There could be several factors able to explain this discrepancy. The first can be potentially related to the pilot flame morphology. As mentioned above, the pilot jets are numerically characterized by an intense heat release in a very limited region. If, for any reason, the reaction rate is overpredicted, the too high fuel consumption limits the possibility for H_2 to be transported toward the methane mixture. In the latter condition, the premixed mixture could surely benefit of H_2 reactivity favoring the premixed flame length reduction. From this point of view, a boundary condition that could have an impact on this mechanism is the heat transfer coefficient applied at the quartz, parameter that could be affected by some uncertainties. At this purpose, an additional analysis is performed imposing an external heat transfer coefficient equal to 100 W/m^2 K, about three times the value applied in the reference case. This boundary condition change could potentially lead the pilot flame to interact with colder gas from the outer recirculation zone (see Fig. 5), eventually leading to a more lifted pilot with higher amount of unburnt H_2 and radicals interacting with the main.

The second factor could be associated with a nonperfect setting of the combustion model. So, an additional simulation is performed adopting a number of points into the flame front thickness equal to $N = 8$ with the goal to verify any improvement due to a rising of the species diffusivity. On the other side, values of $N < 4$ would lead to thickening factors too low and not recommended in literature, and it is decided not to investigate this range.

Figure 7 reports the results of this sensitivity analysis again looking at the heat release rate distribution on the midplane of the combustor. With respect to the reference case (Fig. 7(*a*)), the

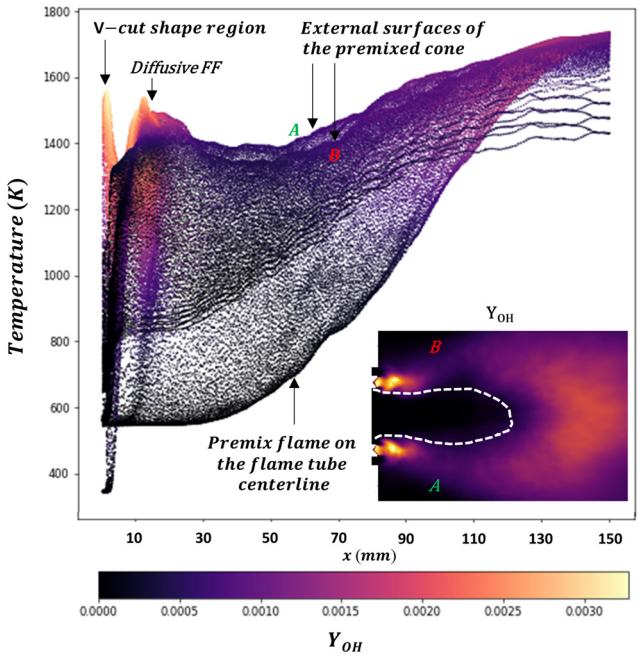

Fig. 9 Scatter plot of mean temperature (in the middle plane) function of the axial coordinate. The OH mass fraction helps to understand the role of the pilot in the premixed flame stabilization.

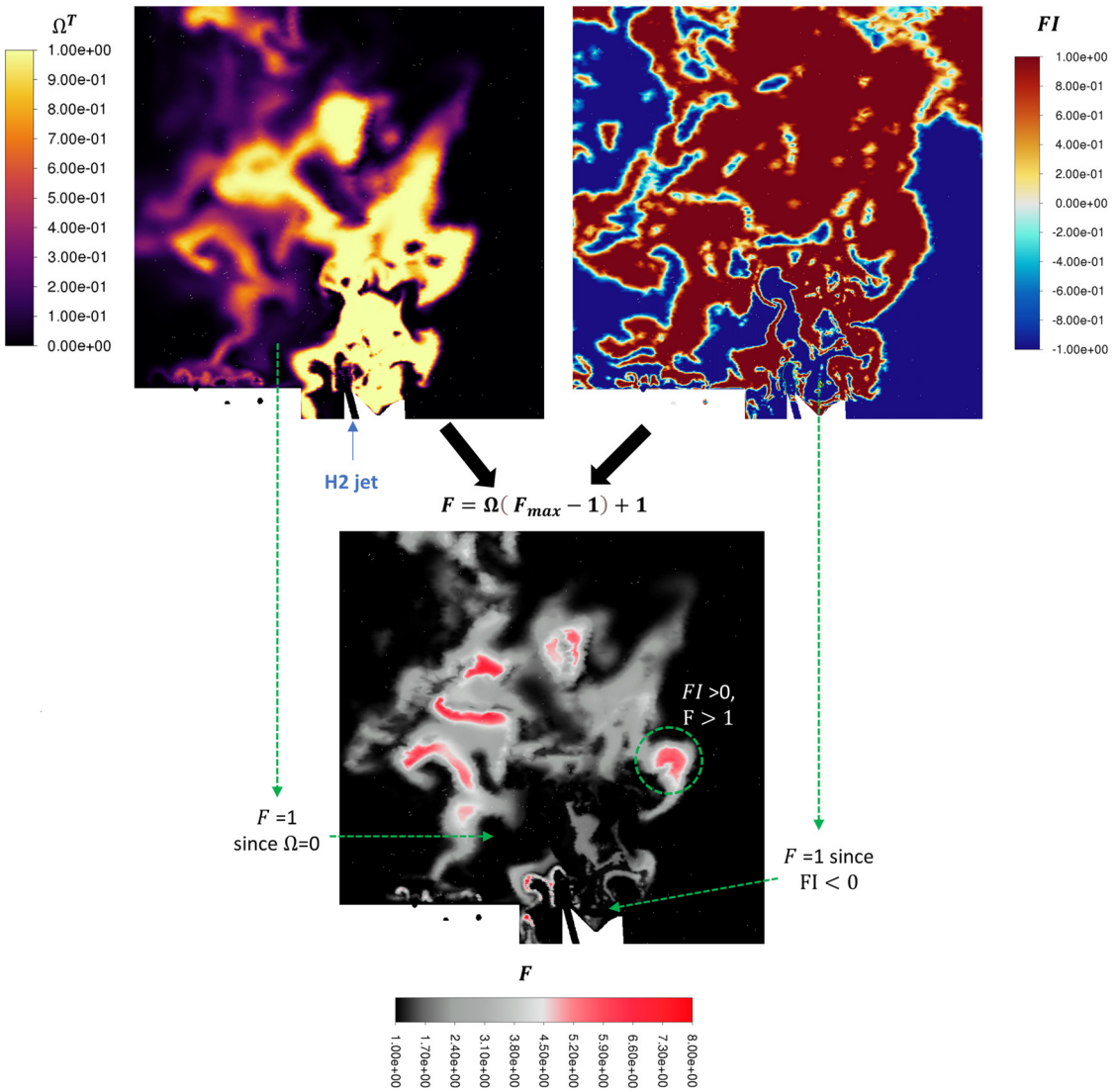

Fig. 10 Correlation between the flame sensor Ω^T, the FI, and the thickening factor *F*

increased external heat transfer coefficient applied on the quartz does not have an impact on the pilot flame that remains compact close to the hydrogen injection. Instead, the higher heat loss produces a less reactive premixed flame front characterized by a lower peak of heat release and an even lifted flame. Also, an enhanced heat release in radial direction can be noticed compared to both the reference case and the experimental map.

The sensitivity to the combustion model setting (Fig. 7(*c*)) reveals that the pilot flame is not affected at all by this modification due to the diffusive combustion regime, as it will be discussed later. Conversely, the premixed flame front gets slightly elongated since its root moves further downstream and the zero-HRR region located in the middle of the two flame fronts along the flame tube axis gets more extended with respect to the reference case. Even the intensity of the heat release peak is subjected to a drop. So, it can be stated that this sensitivity study does not lead to the identification of a potential lack in the boundary condition setting, being the reference case the best against the experimental measurements. One last factor able to explain the misprediction of the premixed flame front is related to the use of pure methane as surrogate of the natural gas that has a non-negligible C_{2+} content. As demonstrated by Romano et al. [17] investigating the same design, the flame position can be affected by C_{2+}: the higher resistance of ethane and propane to the stretch surely leads to a shorter flame.

The contour plot of the time-averaged FI reported in Fig. 8 highlights that the two flame fronts are characterized by opposite regimes. Regarding the H_2-pilots, the combustion is dominantly diffusive: looking at the close-up showed on the bottom part of the figure, it can be seen that the FI ranges from −1 right after the fuel injection, up to –0.2 few millimeters downstream the delivery points. In the latter region, the concentration of H_2 drops practically to zero, as depicted by its mass fraction isolines and demonstrating that the hydrogen flame is extremely short. The pilot regions are followed by a smooth transition toward the premixed regime moving along the axial coordinate of the combustor. Eventually, the methane coming from the main is oxidized burning in premix mode and along a lean combustion, as it can be seen from the highly extended region with a positive FI in the central part of the primary zone and from the corresponding Y_{CH4} isoline, respectively. The analysis of the FI demonstrates that the proposed combustion model is crucial when different regions of the primary zone are interested by multiple oxidation regimes.

The role played by the pilot flame in the stabilization of the main premixed flow can be investigated also through the analysis of Fig. 9. Here, the scatter plot of the mean temperature as a function of the normalized axial coordinate of the flame tube is reported with each point colored by the OH-radical mass fraction. The pilot region is characterized by two different peaks. Moving in *x* direction, the first one corresponds to the high temperature in the V-cut shape where

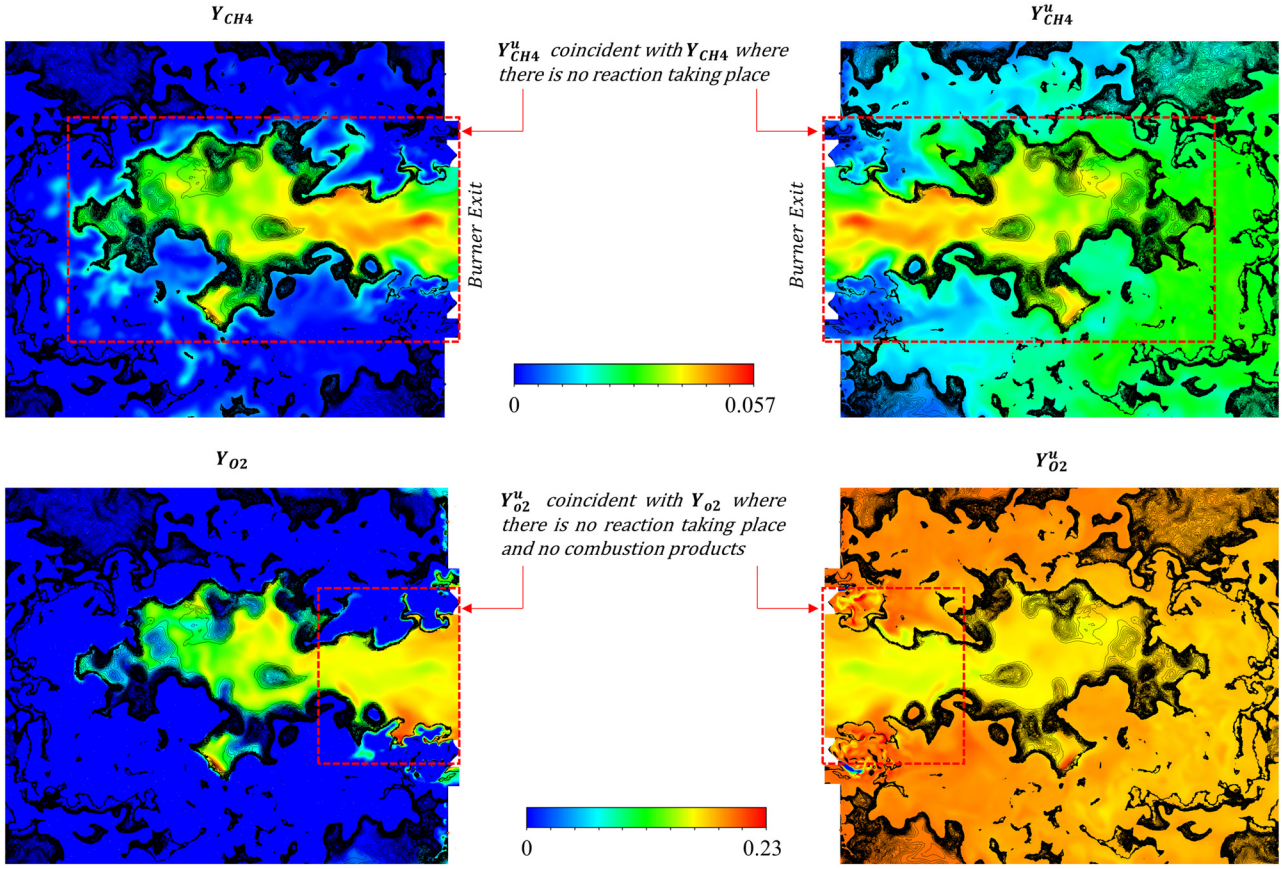

Fig. 11 Comparison between instantaneous species mass fraction Y_n (left) and reconstructed unburnt mass fraction Y_n^u (right). Top row refers to CH_4, and bottom row refers to O_2. The isolines refer to the flame sensor Ω^T with value between 0 and 0.1, helpful to detect the unburnts.

the hot gases coming from the pilot combustion can recirculate. The second peak is related to the H_2 combustion itself right after the injection. Both these peaks have the highest concentration of OH. This radical (as well the others generated from H_2 combustion) is then transported downstream. Focusing on the external parts of the surface delimiting the unburnt premixed flame (A and B in the Y_{OH} contour plot of Fig. 9), both Y_{OH} and the temperature decrease initially, but eventually they start rising again moving forward. It is in this zone that the radicals start igniting the premixed mixture, producing a new rise of temperature and OH concentration. The consequent combustion of CH_4 leads to the absolute maximum of temperature and a new local maximum of OH in the centerline of the combustor.

Combustion Model Verification. In this section, the attention will be focused on the combustion model with the goal to show the way it works from a practical perspective. The first aspect to be presented regards the switch from the FR to the TFM closure, according to the TFM extension presented above. Figure 10 reports the correlation among the flame sensor Ω^T, the FI, and, eventually, on the thickening factor F (and the efficiency function E). The instantaneous contour plots are related to the pilot region but the same considerations are obviously valid also for the premixed flame.

Ω^T represents the first filter applied by the combustion model: according to Eq. (5), in the regions where its value is zero, the thickening factor is not applied at all. Conversely, where the reaction rate of the reference reaction is above zero, the FI acts as the second filter. For example, the FI is dominantly negative in the v-cut region and, as a consequence, here the thickening factor is imposed equal to 1. Some other zones, mainly downstream the injection hole, are instead characterized by a positive flame index. Depending on the spatial resolution of the mesh in these locations and the local laminar flame thickness, F reaches a maximum of 8.

The second aspect of the combustion model to be analyzed concerns the unburnt properties calculation starting from the elemental mass fraction, coming from the solution of the system of equations summarized in Eq. (9). At this scope, Fig. 11 compares the results in terms of CH_4 and O_2, showing the instantaneous mass fraction from the CFD solution on the left side and the reconstructed mass fraction on the right one. Obviously, the same considerations can also be extended to H_2 but its fast consumption (see Fig. 7) would limit the postprocessing to a very narrow region where the comparison is not so meaningful. In Fig. 11, the isolines of the flame sensor Ω^T with value between 0 and 0.1 are used to detect the regions that are not affected by the reaction process. Looking at the main flow coming from the burner, these isolines are helpful to isolate the unburnt mixture. In terms of reconstructed Y^u_{CH4}, it can be observed that inside this region the solution coincides with the Y_{CH4} from the CFD. This demonstrates the correct implementation of the model: since there is no reaction in this zone, the reconstructed mass fraction can derive only from the actual CH_4. Conversely, outside the unburnt region, the Y^u_{CH4} is always higher than Y_{CH4} since the radicals and the other intermediate species partially derives from CH_4 combustion. In terms of oxygen, the perfect match between Y_{O2} and Y^u_{o2} is only limited in those cells that are not involved in any reaction and where there is no combustion product as well. In fact, when the latter condition is verified, the reconstructed oxygen mass fraction is influenced by the oxygen contained in the radicals and combustion products. Looking at the bottom row of Fig. 11, it can be seen that the only zone where these two conditions are verified is limited to few millimeters downstream the burner exit. Right after, the premixed flow coming out from the burner is influenced by the presence of intermediate species/unburnt that lead to the rising of

Y^u_{o2}. To be noted that the assessment of Y^u_{o2} is not necessary for the calculation of the laminar properties of the mixture. It demonstrates that the presented procedure can also be a valid postprocessing tool to understand where a given species concentration derives from.

Conclusions

In this paper, a new methodology to simulate dual-gas configurations has been presented. The method is implemented along a species transport model with the closure of the transport equations conditioned by the local combustion regime. While the diffusive regime leads to a finite rate closure, the premixed part of the combustion, treated according to the thickened flame model, needs to consider the right mixture properties to properly calculate both the laminar flame speed and thickness. This is particularly important when fuel gases with quite different properties like methane and hydrogen are employed. A new procedure leveraging the local elemental mass fraction to retrieve the unburnt mixture from which the mixture properties are quantified has been presented and validated. An atmospheric test rig operating with a pilot fuel line fed with H_2 and a main fed by CH_4 has been employed at this purpose. The validation of the combustion model reveals a good agreement in terms of detection of the flame stabilization mechanisms, especially regarding the pilot jets, while an overprediction of the premixed flame length can be observed. The numerical solution has been finally employed to better investigate the different combustion regimes involving the piloted hydrogen and the premixed flame. Additionally, a focus is dedicated to the interaction between the two flame fronts and how the pilot helps to stabilize the main flame. The last part of the paper has been used to present how the combustion model practically works. The switch from the finite rate to the TFM closure depending on the local flame index value has been showed as well as the recalculation of the unburnt species concentration from which the laminar properties are retrieved.

Acknowledgment

The project TRANSITION (fuTure hydRogen Assisted gas turbiNeS for effective carbon capTure IntegratiON) has received funding from the European Union's Horizon Europe research and innovation programme under the Grant Agreement No. 101069665. Views and opinions expressed are however those of the author(s) only and do not necessarily reflect those of the European Union. Neither the European Union nor the granting authority can be held responsible for them.

Funding Data

- European Union's Horizon Europe research and innovation programme (Grant Agreement No. 101069665).

Data Availability Statement

The datasets generated and supporting the findings of this article are obtainable from the corresponding author upon reasonable request.

Nomenclature

Latin Letters

D = species diffusivity (m^2/s)
E = efficiency function
F = thickening factor
n_f = number of point used to discretize the variability range of the fuel
n_{ox} = number of point used to discretize the variability range of the oxidizer
s_l^0 = laminar flame speed (m/s)
W = molecular weight (kg/mol)
Y = mass fraction
Z = elemental mass fraction

Greek Symbols

α = combustion model constant
Γ = combustion model constant
∇ = gradient operator
φ = vector of the species mass fractions
Φ = equivalence ratio
Ω = flame sensor
$\dot{\omega}$ = reaction rate (kg/m^3 s)

Subscripts/Superscripts

l = laminar
max = referred to the thickening factor
T = referred to a tabulated value
0 = refers to the flame without thickening
1 = refers to the flame with thickening

Acronyms

CFD = computational fluid dynamics
CFL = Courant–Friedrichs–Lewy number
FI = flame index
FR = finite rate
GT = gas turbine
LBO = lean blow-out
LES = large-eddy simulation
LFS = laminar flame speed
LFT = laminar flame thickness
N = number of points in the flame thickness
PIV = particle image velocimetry
TFM = thickened flame model
UDF = user defined function

References

[1] Mira, D., Pérez-Sánchez, E. J., Borrell, R., and Houzeaux, G., 2023, "HPC-Enabling Technologies for High-Fidelity Combustion Simulations," Proc. Combust. Inst., **39**(4), pp. 5091–5125.
[2] Pérez Arroyo, C., Dombard, J., Duchaine, F., Gicquel, L., Martin, B., Odier, N., and Staffelbach, G., 2021, "Towards the Large-Eddy Simulation of a Full Engine: Integration of a 360 Azimuthal Degrees Fan, Compressor and Combustion Chamber. Part I: Methodology and Initialization," J. Global Power Propul. Soc., pp. 1–16.
[3] Colin, O., Ducros, F., Veynante, D., and Poinsot, T., 2000, "A Thickened Flame Model for Large Eddy Simulations of Turbulent Premixed Combustion," Phys. Fluids, **12**(7), pp. 1843–1863.
[4] Wang, G., Boileau, M., and Veynante, D., 2011, "Implementation of a Dynamic Thickened Flame Model for Large Eddy Simulations of Turbulent Premixed Combustion," Combust. Flame, **158**(11), pp. 2199–2213.
[5] Agostinelli, P. W., Laera, D., Chterev, I., Boxx, I., Gicquel, L., and Poinsot, T., 2022, "On the Impact of H_2-Enrichment on Flame Structure and Combustion Dynamics of a Lean Partially-Premixed Turbulent Swirling Flame," Combust. Flame, **241**, p. 112120.
[6] Laera, D., Agostinelli, P. W., Selle, L., Cazères, Q., Oztarlik, G., Schuller, T., Gicquel, L., and Poinsot, T., 2021, "Stabilization Mechanisms of CH_4 Premixed Swirled Flame Enriched With a Non-Premixed Hydrogen Injection," Proc. Combust. Inst., **38**(4), pp. 6355–6363.
[7] Riber, E., Cuenot, B., and Poinsot, T., 2019, "Introducing Chemical Kinetics Into Large Eddy Simulation of Turbulent Reacting Flows," Comput. Aided Chem. Eng., **45**, pp. 899–936.
[8] Castellani, S., Meloni, R., Orsino, S., Ansari, N., Yadav, R., Bessette, D., Boxx, I., and Andreini, A., 2023, "High-Fidelity H_2–CH_4 Jet in Crossflow Modelling With a Flame Index-Controlled Artificially Thickened Flame Model," Int. J. Hydrogen Energy, **48**(90), pp. 35291–35304.
[9] Cuenot, B., Shum-Kivan, F., and Blanchard, S., 2021, "The Thickened Flame Approach for Non-Premixed Combustion: Principles and Implications for Turbulent Combustion Modeling," Combust. Flame, **239**, p. 111702.
[10] Aniello, A., Laera, D., Marragou, S., Magnes, H., Selle, L., Schuller, T., and Poinsot, T., 2023, "Experimental and Numerical Investigation of Two Flame Stabilization Regimes Observed in a Dual Swirl H_2-Air Coaxial Injector," Combust. Flame, **249**, p. 112595.
[11] Meloni, R., Orsino, S., Ansari, N., Yadav, R., Bessette, D., Castellani, S., Nassini, P. C., Andreini, A., and Boxx, I., 2023, "Partially Premixed Hydrogen-Methane Flame Simulations at Relevant Gas Turbine Conditions With a Thickened Flame Model Enhancement," ASME Paper No. GT2023-102427.

[12] Mocquard, C., Laera, D., Dombard, J., and Poinsot, T., 2023, "A Two-Step Chemical Scheme for Auto-Igniting and Propagating Kerosene Flames at Reheat Conditions," Combust. Flame, **248**, p. 112558.
[13] Durand, L., and Polifke, W., 2007, "Implementation of the Thickened Flame Model for Large Eddy Simulation of Turbulent Premixed Combustion in a Commercial Solver," ASME Paper No. GT2007-28188.
[14] University of California at San Diego, 2024, "Chemical-Kinetic Mechanisms for Combustion Applications," San Diego Mechanism Web Page, Mechanical and Aerospace Engineering (Combustion Research), University of California at San Diego, San Diego, CA, accessed Sept. 23, 2024, https://web.eng.ucsd.edu/mae/groups/combustion/mechanism.html
[15] Goodwin, D. G., Speth, R. L., Moat, H. K., and Weber, B. W., 2018, "Cantera: An Object-Oriented Software Toolkit for Chemical Kinetics, Thermodynamics, and Transport Processes," Cantera, accessed Sept. 23, 2024, https://cantera.org/
[16] Meloni, R., Andreini, A., and Nassini, P. C., 2022, "A Novel Large-Eddy Simulation-Based Process for NOx Emission Assessment in a Premixed Swirl Stabilized Combustion System," ASME J. Eng. Gas Turbines Power, **144**(1), p. 011010.
[17] Romano, S., Meloni, R., Riccio, G., Nassini, P. C., and Andreini, A., 2021, "Modeling of Natural Gas Composition Effect on Low NOx Burners Operation in Heavy Duty Gas Turbine," ASME J. Eng. Gas Turbines Power, **143**(3), p. 031018.
[18] Meloni, R., Gori, S., Andreini, A., and Nassini, P. C., 2022, "CO Emission Modeling in a Heavy Duty Annular Combustor Operating With Natural Gas," ASME J. Eng. Gas Turbines Power, **144**(1), p. 011011.
[19] Rochette, B., Collin-Bastiani, F., Gicquel, L., Vermorel, O., Veynante, D., and Poinsot, T., 2018, "Influence of Chemical Schemes, Numerical Method and Dynamic Turbulent Combustion Modeling on LES of Premixed Turbulent Flames," Combust. Flame, **191**, pp. 417–430.
[20] Nicoud, F., and Ducros, F., 1999, "Subgrid-Scale Stress Modelling Based on the Square of the Velocity Gradient Tensor," Flow, Turbul., Combust., **62**(3), pp. 183–200.
[21] Boudier, G., Gicquel, L. Y. M., and Poinsot, T. J., 2008, "Effects of Mesh Resolution on Large Eddy Simulation of Reacting Flows in Complex Geometry Combustors," Combust. Flame, **155**(1–2), pp. 196–214.
[22] Pope, S. B., 2004, "Ten Questions Concerning the Large Eddy Simulations of Turbulent Flows," New J. Phys., **6**, p. 35.